GDCh

Research Article

Angewandte
International Edition Chemie
www.angewandte.org

Check for updates

Cyclohexanone Oxime Electrosynthesis | Hot Paper

A Heterodimeric Cluster-Based Pair Catalyst for Electrochemical Synthesis of Cyclohexanone Oxime

Tongxin Song+, Chenyang Shen+, Yiqi Tian, Qingxi Zhai, Shisi Tang, and Yan Zhu*

Abstract: Heterogeneous catalysts are complex chemical ecosystems, where various functional units execute their individual responsibilities to together complete a catalysis ensemble. Here, we report a dinuclear catalyst originated from two molecular-purity monomers including an atomically precise $Ag_4Pd_2(SR)_8$ cluster and a polyoxotitanium $Ti_4O_2(TBC[4])_2(^iPrO)_4$ cluster that are eventually paired off by the bridging sulfur. The heterodimeric catalyst with a unique interface consisted of the Ti—S—metal (metal = Pd and Ag) motifs exhibits selective recognition for nitrogen sources, thereby achieving high performances for the electrochemical synthesis of cyclohexanone oxime. The nitrate is favorably deoxygenated on the metal sites to generate nitrite, followed by the flipping of nitrite at the Ti—S—metal interface and the stepwise reduction of nitrite on the Ti site to produce hydroxylamine. Sequentially, a spontaneous coupling from hydroxylamine and cyclohexanone proceeds to construct the C=N bond for cyclohexanone oxime. Using this combination of distinct functional modules into one catalyst, we develop a strategy for heterogeneous catalysts being designed to increase the substrate conversion while simultaneously increasing the target product selectivity.

Introduction

Cyclohexanone oxime (CHOX) is the main feedstock for the industrial production of nylon-6, and more than 90% of the global caprolactam is produced from CHOX rearrangement.[1,2] Thus the expanding demand imposes stringent requirements for CHOX synthesis. Recently, the electrochemical synthesis of CHOX has attracted extensive research interest via utilizing cyclohexanone (CHO) to capture the crucial hydroxylamine (NH_2OH) species generated

[*] T. Song+, C. Shen+, Y. Tian, Q. Zhai, S. Tang, Prof. Y. Zhu
Key Laboratory of Mesoscopic Chemistry of Ministry of Education,
State Key Laboratory of Coordination Chemistry, School of
Chemistry and Chemical Engineering, Nanjing University, Nanjing,
China 210093
E-mail: zhuyan@nju.edu.cn

[+] Both authors contributed equally to this work.

🖥 Additional supporting information can be found online in the
Supporting Information section

during the electroreduction reaction of nitrate.[3–6] As shown in Figure 1a, nitrate (NO_3^-) is used as the nitrogen source, and undergoes the deoxygenation process to progressively generate nitrite (NO_2^-) and NO, followed by either the hydrogenation reaction to produce NH_2OH or the N—O bond breaking and hydrogenation to produce ammonia (NH_3).[7,8] The NH_2OH desorbs from the catalyst surface and dehydrates with CHO in the solution by nucleophilic condensation to produce CHOX.[9,10] Under the electroreduction conditions, it is challenging for the attainment of the catalysts with high conversion of nitrate and high selectivity of CHOX, since NO_3^- is highly susceptible to retention as NO_2^- without further reduction,[11] as well as the N—O bond breakage usually occurs and is further hydrogenated to NH_3.[12,13] It is therefore highly required for the discovery of new catalysts to increase the nitrate conversion while simultaneously increasing the CHOX selectivity.

Atomically precise metal clusters and polyoxometalate clusters have gained momentum over the past decade for the development of atomic-level catalysis systems,[14–20] since their total structures could be solved by single crystal X-ray crystallography. Based on these clusters with determined structures, catalytic active sites and active species can be identified or proposed.[21–24] The issues are very challenging yet highly important for typical heterogeneous catalysts such as supported metal catalysts, because too many factors have to be considered including the interplay between the metal and the support.[25–27] In retrospect requirements on electrochemical synthesis of cyclohexanone oxime, we therefore recognized that atomically precise clusters might provide access to an ideally well-defined catalyst that couples increase in substrate conversion with increased CHOX selectivity.
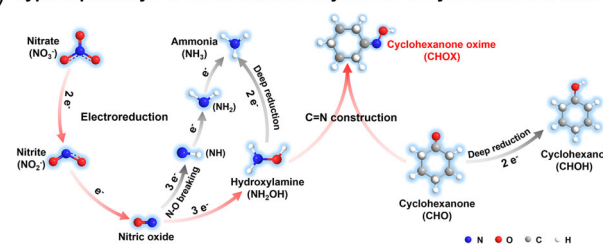
To examine this possibility, we initially measured catalytic performances of a series of metal clusters including Au, Ag, Cu and their alloys for CHOX synthesis (Figure S1). An interesting phenomenon was observed that the $Ag_4Pd_2(SR)_8$ (SR = 2,4-dimethylthiophenol) cluster catalyst exhibited a high Faradaic efficiency (FE) for NO_2^-, with 100% selectivity for CHOX in organic products. We then screened titanium dioxide and polyoxotitanium clusters in this electrochemical process and found that the titanium-oxide compounds showed a very low current density in the NO_3^- and CHO system, in which NO_3^- was readily converted to NH_4^+ (Figure S2a). Notably, the FE of NH_4^+ for the $Ti_4O_2(TBC[4])_2(^iPrO)_4$ cluster (hereafter Ti4-^iPrOH; ^iPrO = isopropoxy group; TBC[4] = 4-tert-butylcalix[4]arene) decreased when NO_2^- was used as the nitrogen source, and the FE of CHOX slightly increased compared to the NO_3^- source system

Angew. Chem. Int. Ed. **2025**, e202507569 (1 of 8)
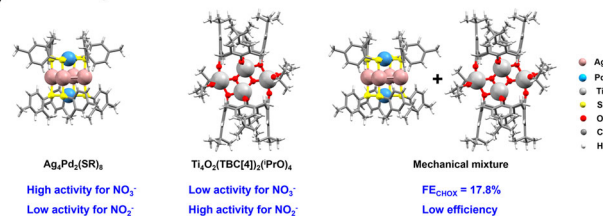
© 2025 Wiley-VCH GmbH

Figure 1. Electrochemical synthesis of cyclohexanone oxime and our initial study. a) Schematic diagram for electrochemical synthesis of cyclohexanone oxime using nitrate as the nitrogen source. b) Initial studies in this work including total structures and mechanical mixture of $Ag_4Pd_2(SR)_8$ and Ti_4-^iPrOH and their corresponding catalytic performances.

(Figure S2b). The results implied that the Ti_4-^iPrOH cluster had a high activity for the NO_2^- reduction. Naturally, a question was whether the bifunctional complex composed from the $Ag_4Pd_2(SR)_8$ cluster and the Ti_4-^iPrOH cluster could control the reduction of NO_3^- on the former to produce NO_2^-, followed by further reduction of NO_2^- on the latter. Frustrated by the performance of the mechanical mixture of the two clusters, it showed a very low efficiency with 17.8% FE of CHOX (Figure 1b). Therefore, we envisioned that high activity and high selectivity would merge via a particular interfacial domain consisted of the two active sites severally originated from $Ag_4Pd_2(SR)_8$ and Ti_4-^iPrOH functional units.

Results and discussion

Inspired by our novel heterodimeric catalyst with the formation of Ti—S—metal interfacial motifs (e.g., Ti—S—Pd and Ti—S—Ag) consisted of $Ag_4Pd_2(SR)_8$ and Ti_4-^iPrOH monomers, the electrosynthesis of CHOX in alkaline electrolyte reached a selectivity of 100% and a Faradaic efficiency of 68.5%, outperforming most catalysts reported under comparable conditions (Table S1). A typical synthesis and chemical conformation of the heterodimeric catalyst labeled as Ag_4Pd_2-S-Ti_4 were outlined in Figure 2. Firstly $Ag_4Pd_2(SR)_8$ and $Ti_4O_2(TBC[4])_2(^iPrO)_4$ were prepared and their structures were shown in Figure 2a and Figure S3,[28,29] where four Ag atoms of $Ag_4Pd_2(SR)_8$ formed a quadrilateral plane, with one Pd atom at the top and one at the bottom, projected in the center of the quadrilateral, and each pair of Ag and Pd atoms was bridged by a thiol ligand; four Ti atoms of Ti_4-^iPrOH were located in a rhombic plane, with one calixarene capping at the top and bottom, and two ^iPrO groups on the left and right

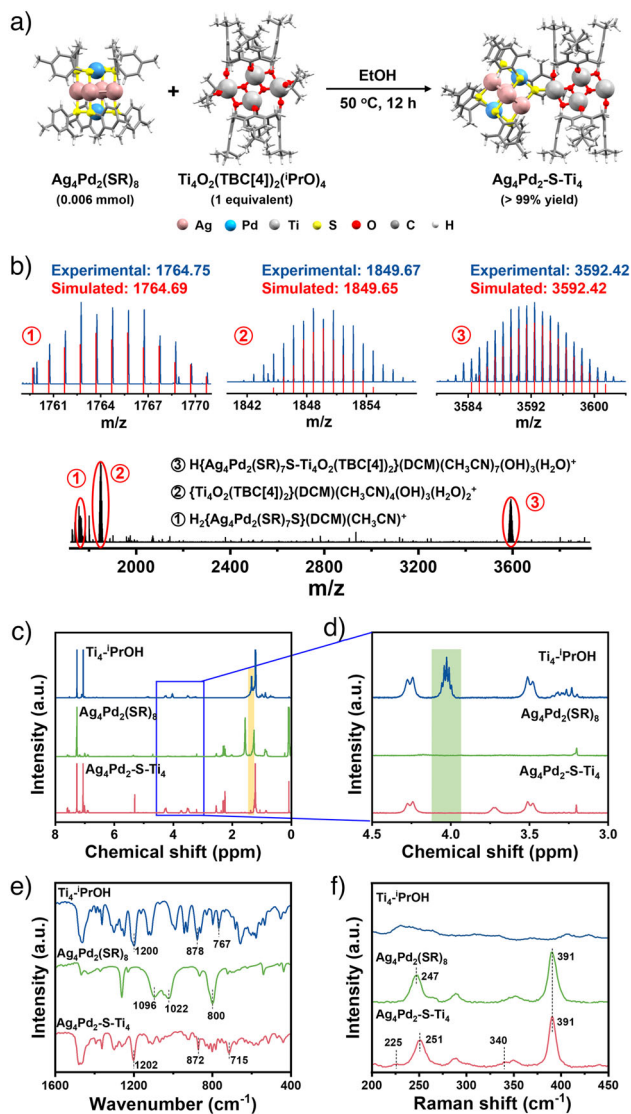**Figure 2.** Chemical synthesis and constitution of heterodimeric Ag_4Pd_2-S-Ti_4 catalyst. a) Schematic diagram of the preparation of the Ag_4Pd_2-S-Ti_4 catalyst using $Ag_4Pd_2(SR)_8$ and Ti_4-^iPrOH as precursors in the ethanol at 50 °C for 12 h. b) ESI-MS profiles of the Ag_4Pd_2-S-Ti_4 sample. c) ^1H NMR spectra of the three samples. d) Enlarged view of the blue box in Figure 2c. e) FTIR spectra and f) Raman spectra of the three samples.

Ti atoms, respectively. Then, the reaction of as-prepared $Ag_4Pd_2(SR)_8$ and Ti_4-^iPrOH was proceeded in the ethanol to obtain the heterodimeric catalyst. Figure 2b showed the electrospray ionization mass spectra (ESI-MS) of the catalyst in positive ion mode with acetonitrile (CH_3CN) as the solvent. The peak with m/z of 3592.42 was assigned to $H\{Ag_4Pd_2(SR)_7S$-$Ti_4O_2(TBC[4])_2\}(DCM)(CH_3CN)_7(OH)_3(H_2O)^+$. The two peaks at 1764.75 and 1849.67 were assigned to $H_2\{Ag_4Pd_2(SR)_7S\}(DCM)(CH_3CN)^+$ and $\{Ti_4O_2(TBC[4])_2\}(DCM)(CH_3CN)_4(OH)_3(H_2O)_2^+$, respectively. This MS result suggested that the catalyst might be assigned to a pair of $Ag_4Pd_2(SR)_7S$ and $Ti_4O_2(TBC[4])_2$, in which one thiolate ligand and all the ^iPrO groups were removed. Based on the molecular formula of the catalyst,

we recognized that it was thermodynamically favorable to produce a bare S atom by C—S bond breaking in $Ag_4Pd_2(SR)_8$ cluster (Figure S4) and the iPrO groups of $Ti_4O_2(TBC[4])_2(iPrO)_4$ were readily kinetically driven off in the presence of ethanol (Figure S5) to produce the unsaturated Ti atoms, thereby that the bare S atom and unsaturated Ti atom naturally combined to form the Ti—S bonds in this catalyst. Due to the inherent links of the S—Pd and S—Ag in the $Ag_4Pd_2(SR)_8$, the Ti—S—Pd and Ti—S—Ag bonds should exist in the catalyst as described as the Ag_4Pd_2-S-Ti_4.

We further identified the conformation of the Ag_4Pd_2-S-Ti_4 catalyst through a series of spectroscopy studies. Nuclear magnetic resonance (^1H NMR) spectra of the Ag_4Pd_2-S-Ti_4 catalyst showed that the dichotomous peaks at 1.3 ppm and the multiple peaks at 4.0 ppm assigned to the hydrogen response of isopropoxy groups were not observed (Figure 2c,d), compared to those of the $Ag_4Pd_2(SR)_8$ and Ti_4-iPrOH monomers (For Ti_4-iPrOH, the signals at 1.2, 4.3 and 3.5 ppm, as well as 7.0 ppm were respectively assigned to tert-butyl group (—C_4H_9), methylene (—CH_2—), and benzene ring H; for $Ag_4Pd_2(SR)_8$, the signal at 6.7~7.2 ppm was assigned to the benzene ring H and the signal at 2.3 ppm was related to the —CH_3 from the ligands.). Fourier transform infrared (FTIR) spectra also revealed the formation of the Ti—S bonds in the Ag_4Pd_2-S-Ti_4. As shown in Figure 2e and S6, the IR bands of Ti_4-iPrOH at 1200, 878, and 767 cm^{-1} were assigned to C—O—Ti, phenyl—O—Ti, and Ti—O—Ti species,[29,30] respectively. The bands of $Ag_4Pd_2(SR)_8$ at 1096, 1022, and 800 cm^{-1} were attributed to C—S stretching vibration, C—H bending vibration and C—H out-of-plane bending vibration on the benzene ring,[31] respectively. For the Ag_4Pd_2-S-Ti_4 sample, the band at 715 cm^{-1} assigned to the Ti—S bond appeared,[32] while the band corresponding to C—O—Ti (1202 cm^{-1}) deformed and the band from phenyl-O-Ti slightly shifted to 872 cm^{-1}.[29,30] From Raman spectra of the three samples (Figure 2f), the Ti_4-iPrOH did not exhibit obvious responses at 200–450 cm^{-1}, while the bands at 391 cm^{-1} from in-plane bending vibration of the methyl groups of benzene ring were observed for both of $Ag_4Pd_2(SR)_8$ and Ag_4Pd_2-S-Ti_4.[33] The response at 247 cm^{-1} in $Ag_4Pd_2(SR)_8$ belonged to the metal-S,[34] while the band shifted to 251 cm^{-1} in Ag_4Pd_2-S-Ti_4. Specially, the two bands at 225 and 340 cm^{-1} assigned to the vibration of Ti—S bonds only appeared in the Ag_4Pd_2-S-Ti_4 case.[35,36] The Ag_4Pd_2-S-Ti_4 catalyst also showed different metal charge states from its monomers analyzed by X-ray photoelectron spectroscopy (XPS). The binding energies (BEs) of Pd of the Ag_4Pd_2-S-Ti_4 shifted towards higher BEs, while the BEs of Ag shifted to lower BEs, compared to the monomers (Figure S7), reflecting that the electronic structures of Pd and Ag of the coupled catalyst were distinct from its monomers. The changes in the Ti charge state were also monitored by X-ray absorption near-edge structure (XANES) experiments (Figure S8a), which suggested that the Ti charge state of Ag_4Pd_2-S-Ti_4 appeared to be more positive than that of Ti_4-iPrOH but less positive than that of TiO_2. The local coordination environment of Ti was further revealed by extended X-ray absorption fine structure (EXAFS) studies.

In Figure S8b, Ti_4-iPrOH showed a Ti—O contribution peak at 2.02 Å. After coupling with $Ag_4Pd_2(SR)_8$ cluster to form Ag_4Pd_2-S-Ti_4, a weak peak at 2.62 Å was assigned to Ti—S bonds,[37] while a prominent peak at 1.48 Å was related with Ti—O bonds (more details in Figure S9 and Table S2).[38]

Overall, we identified the chemical construction of the Ag_4Pd_2-S-Ti_4 catalyst that elaborately coupled the metal cluster with the polyoxometalate cluster to construct the interfacial domain of Ti—S—metal (metal = Pd and Ag), thereby tailoring the proximity of the two functional monomers. In addition, the total energy of the whole system of Ag_4Pd_2-S-Ti_4 model remained stable during ab initio molecular dynamics (AIMD), further suggesting that the structural identification of the heterodimeric cluster was reasonable (Figure S10).

We next evaluated the catalytic performance for electrochemical synthesis of CHOX under optimized conditions (Figure S11). The $Ag_4Pd_2(SR)_8$ showed a distinct reduction peak at $-0.9 \sim -1.15$ V versus Ag/AgCl, which was attributed to the initial reduction of NO_3^- (Figure S12). The reduction peak of Ag_4Pd_2-S-Ti_4 at this position decreased and shifted to more negative potential, while Ti_4-iPrOH hardly displayed a reduction peak. The polarization curves of the three catalysts in different electrolyte solutions were also compared: when only NO_3^- was added into the KOH electrolyte (blue lines in Figure S13), the currents were much higher than the cases without NO_3^- (yellow lines in Figure S13), indicating that the three catalysts could catalyse the NO_3^- reduction. It was noteworthy that the onset potential of NO_3^- reduction by $Ag_4Pd_2(SR)_8$ was -0.9 V versus Ag/AgCl, while that by Ti_4-iPrOH was -1.5 V versus Ag/AgCl. When only CHO was added in the KOH electrolyte (green lines in Figure S13), the three catalysts showed very weak reduction currents, indicating that the three catalysts were not capable of reducing CHO. Moreover, when CHO was presented together with NO_3^- (red lines in Figure S13), the current densities were close to those of the systems with only NO_3^- in KOH, further suggesting that the three catalysts had reduction activities for NO_3^- rather than CHO. The above observations indicated that the stepwise reduction of NO_3^- occurred on the catalyst, while the coupling process of CHO and NH_2OH spontaneity proceeded in the solution.

Figure 3a showed the conversion of CHO and selectivity of CHOX over the Ag_4Pd_2-S-Ti_4 catalyst after continuous 5 h current-time (i-t) testing at different applied potentials (Figure S14). Throughout the whole potential, the selectivity for CHOX ranged from 95.0% to 100%, with up to 89.7% conversion of CHO. NMR analysis and mass spectra of CHO, CHOX and reacted electrolyte indicated that CHOX was really generated in the reaction system (Figure 3b,c). When ^{15}N-labeled $^{15}NO_3^-$ was used as the nitrogen source, the molecular ion peaks showed m/z of 32, 55 and 114, demonstrating that the synthesized CHOX indeed derived from the nitrate source (Figure 3c). Figure 3d–f showed the heatmaps of FEs for different products obtained from the catalytic systems of $Ag_4Pd_2(SR)_8$, Ti_4-iPrOH, and Ag_4Pd_2-S-Ti_4. In Figure 3d, Ag_4Pd_2-S-Ti_4 exhibited much higher FE for CHOX than $Ag_4Pd_2(SR)_8$ and Ti_4-iPrOH, reaching 41.2% at a potential of -1.6 V versus Ag/AgCl. It was noted that
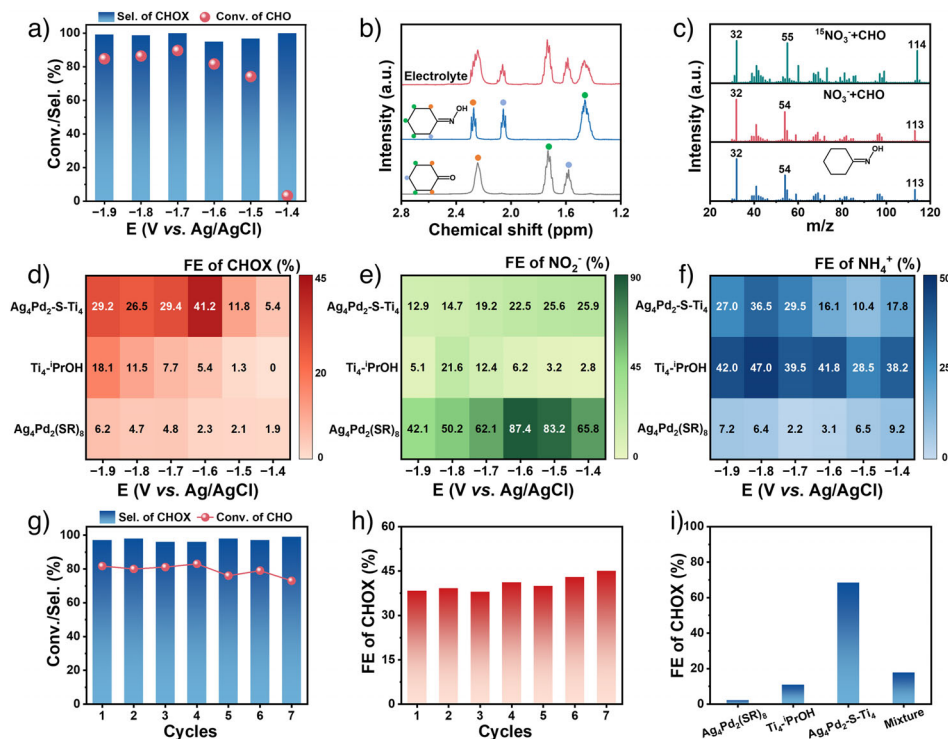
Figure 3. Electrosynthesis of CHOX. a) Potential-dependent CHO conversion and CHOX selectivity for the Ag_4Pd_2-S-Ti_4 catalyst in the solution of 0.4 M KNO_3 and 0.05 M CHO. b) ^1H NMR of Ag_4Pd_2-S-Ti_4 catalyzed electrolyte and standard CHO and CHOX samples. c) Mass spectra of CHOX standard sample, liquid products severally from the electrolyte of NO_3^- reacted with CHO and the electrolyte of ^{15}N-labeled $^{15}NO_3^-$ reacted with CHO using the Ag_4Pd_2-S-Ti_4 catalyst. d)–f) Heatmaps of FEs for CHOX, NO_2^- and NH_4^+ in $Ag_4Pd_2(SR)_8$, Ti_4-^iPrOH and Ag_4Pd_2-S-Ti_4 catalyzed systems. g) Recyclability of Ag_4Pd_2-S-Ti_4 at a potential of −1.6 V versus Ag/AgCl. h) FEs of CHOX over Ag_4Pd_2-S-Ti_4 in seven consecutive cyclic tests at a potential of −1.6 V versus Ag/AgCl. i) FEs of CHOX over $Ag_4Pd_2(SR)_8$, Ti_4-^iPrOH, Ag_4Pd_2-S-Ti_4 and the mechanical mixture of $Ag_4Pd_2(SR)_8$ and Ti_4-^iPrOH, respectively. The experiments were carried out in an electrolyte of 0.5 M KNO_3 and 0.1 M CHO.

$Ag_4Pd_2(SR)_8$ displayed high FEs for NO_2^- over the whole potential range (Figure 3e), due to the difficulty in further reduction of NO_2^-, while Ti_4-^iPrOH exhibited relatively high FEs for NH_4^+ (Figure 3f). Whereas, the FEs for NO_2^- and NH_4^+ of Ag_4Pd_2-S-Ti_4 were relatively low. In addition, 8-hydroxyquinoline colorimetric method quantified NH_2OH in the CHO-containing and CHO-free systems (Figure S15 and S16), which suggested the spontaneous coupling of CHO with NH_2OH for the efficient generation of CHOX. Notably, the Ag_4Pd_2-S-Ti_4 catalyst was quite robust during the catalytic reactions (Figure S17 and S18), thereby exhibiting an excellent recyclability and long-term stability (Figure 3g,h and S19). Inductively coupled plasma mass spectrometry (ICP-MS) analysis of the electrolyte after long-term test showed that the concentrations of Ag, Pd and Ti were 0.14, 0.20, and 0.39 µg L^{-1}, respectively, suggesting no obvious metal leaching occurred on the catalyst during the catalytic reaction. FTIR and Raman spectra further indicated the Ag_4Pd_2-S-Ti_4 catalyst was robust during the long-term reaction (Figure S20). As expected, compared to the mechanically mixed material of $Ag_4Pd_2(SR)_8$ and Ti_4-^iPrOH, the Ag_4Pd_2-S-Ti_4 catalyst exhibited approximately 4-fold increase in FE of CHOX (Figure 3i and S21). More importantly, the catalytic property of Ag_4Pd_2-S-Ti_4 outperformed most catalysts reported (Table S1).

We initiated mechanistic studies to determine the origin of the high performance of the Ag_4Pd_2-S-Ti_4 catalyst. The electrochemically surface area (ECSA) was first tested by electrochemical double-layer capacitance (Figure S22). The fitted double-layer capacitances (C_{dl}) of the three catalysts were 0.56, 0.38, and 0.29 mF cm^{-2}, respectively. Assuming a specific capacitance (C_s) value of 40 µF cm^{-2},[7,8,39] the calculated ECSAs were 14.0 cm^{-2} (Ag_4Pd_2-S-Ti_4), 9.5 cm^{-2} (Ti_4-^iPrOH), and 7.3 cm^{-2} ($Ag_4Pd_2(SR)_8$), respectively, where the largest ECSA of the Ag_4Pd_2-S-Ti_4 catalyst implied the most active sites. The interfacial charge transfer was studied by in situ electrochemical impedance spectroscopy (EIS) to explore the interfacial kinetic behavior of the catalysts.[40,41] The potential-dependent Bode plots with the phase angle as a function of frequency of the three catalysts in the solution of KNO_3 and CHO were shown in Figure 4a–c and corresponding modulus (Z) versus frequency plots were shown in Figure S23. With the increase of cathodic potential, both Ag_4Pd_2-S-Ti_4 and Ti_4-^iPrOH displayed an evolution from a singlet peak to a dichotomous peak (Figure 4a,c), indicating that the two catalytic systems were likely controlled by the charge transfer and diffusion processes at high potentials. In contrast, the $Ag_4Pd_2(SR)_8$ system was potentially controlled by the charge transfer process (Figure 4b). In the low frequency region, the Ag_4Pd_2-S-Ti_4 catalyst developed an inflection point at −0.9 V and the inflection point shifted toward the high frequency region as the potential increased. Meanwhile the corresponding phase angles gradually decreased when the potential increased from
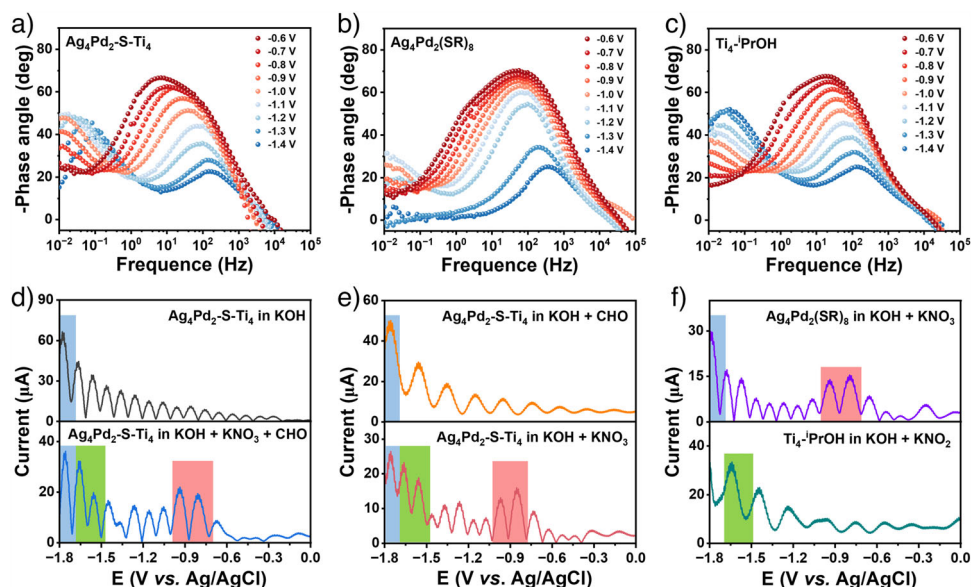
Figure 4. Electrochemical properties and kinetic behaviors of the three catalysts. The potential-dependent Bode phase angle plots over a) Ag_4Pd_2-S-Ti_4, b) $Ag_4Pd_2(SR)_8$, and c) Ti_4-^iPrOH catalysts in the electrolyte containing KNO_3 and CHO. d)–f) The fifth harmonic FTACV curves derived from different electrolyte systems. Frequency = 10 Hz, amplitude = 0.1 V.

−1.1 V, suggesting that the interfacial charge transfer was facilitated at high potentials and the diffusion process became dominant in the system. Additionally, Ti_4-^iPrOH showed an inflection point at −1.3 V in the low frequency region, indicating more negative onset reduction potential on the Ti_4-^iPrOH than that on the Ag_4Pd_2-S-Ti_4. In the high frequency region, the phase angle values of the three catalysts had no significant difference, suggesting that their reaction kinetics were comparable in this region.[42]

Fourier-transformed alternating current voltammetry (FTACV) was performed to indicate the electron transfer of the electrosynthesis of CHOX over the three catalysts in various electrolytes. The higher-order harmonic components of FTACV can avoid non-Faraday process and enable the sensitive detection of potential electron transfer,[43,44] and hence the fifth harmonic components of FTACV were investigated. In KOH solution, the Ag_4Pd_2-S-Ti_4 showed a high current around −1.8 V (blue region in the upper panel of Figure 4d), which represented the catalytic process for hydrogen evolution. Ag_4Pd_2-S-Ti_4 additionally displayed two current peaks in the co-presence of KNO_3 and CHO (green and pink regions in the lower panel of Figure 4d), which corresponded to different electron transfer processes of the NO_3^- reduction.[45–47] When only CHO was presented, Ag_4Pd_2-S-Ti_4 exhibited the current signal only in the blue region (upper panel in Figure 4e), indicating that the catalyst had no ability to catalyze the reduction of CHO and hence its deep reduction product such as cyclohexanol was effectively prevented in the Ag_4Pd_2-S-Ti_4 system. When only NO_3^- was included, Ag_4Pd_2-S-Ti_4 also displayed three reduction current signals (lower panel in Figure 4e), which was similar to the case of KNO_3 and CHO. In contrast, when the $Ag_4Pd_2(SR)_8$ cluster catalyzed the NO_3^- reduction, the obvious responses appeared in the pink and blue regions (upper panel in

Figure 4f), the latter of which was identified as the hydrogen evolution process and the former was speculated possibly from the incomplete reduction of NO_3^-. The Ti_4-^iPrOH cluster exhibited a reduction current in the green region when catalyzing the KNO_2 reduction (lower panel in Figure 4f). Based on the above analysis, we proposed the catalytic mechanism for the electrochemical synthesis of CHOX driven by the Ag_4Pd_2-S-Ti_4 catalyst, in which the Ag_4Pd_2 unit preferentially reduced NO_3^- to NO_2^-, and then NO_2^- was transferred onto the other unit or the interface for further deoxygenation and hydrogenation to produce NH_2OH, finally NH_2OH spontaneously underwent a couple reaction with CHO in the solution to generate CHOX.

We then sought to detect the reaction intermediate species formed in specific electrolytes by experimentally determined the molecular-level reaction pathways of NO_3^- reduction on the Ag_4Pd_2-S-Ti_4 catalyst. Figure 5a and S24a showed the Raman spectra obtained from the Ag_4Pd_2-S-Ti_4 catalyst system in 0.4 M KNO_3 solution with/without CHO. The band at 1045 cm^{-1} was attributed to free NO_3^- species in the solution,[3] overlapping with the vibrational bands of the benzene ring skeleton from the cluster ligands. The weak band at 1004 cm^{-1} was assigned to the vibration of adsorbed *NO_3^- species.[3] With the increase of the cathode potential, the bands at 1284 and 1444 cm^{-1} gradually appeared (Figure S24a), which corresponded to the asymmetric stretching vibration of *NO_2^- group[48] and the stretching vibration of N=O from *NO_2^- group,[49] respectively. The signals at 930 and 1380 cm^{-1} were from the N—O stretching vibration of *NH_2OH species[3] and the symmetric bending vibration of *HNH,[50] respectively, indicating that in the absence of CHO in the reaction, the generated NH_2OH species would be further reduced to *HNH species and finally NH_3 product. When CHO was added into the reaction system
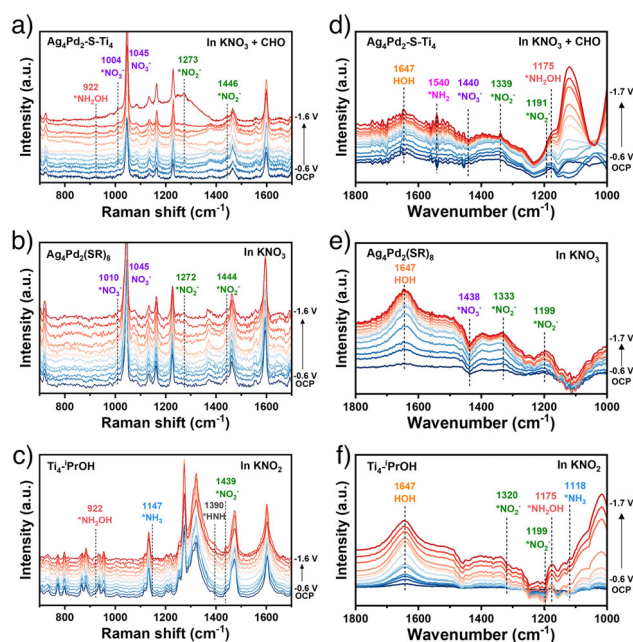
Figure 5. In situ Raman and ATR-FTIR spectra corresponding to the reaction intermediates formed on the catalysts. In situ Raman spectra obtained from a) the Ag_4Pd_2-S-Ti_4 system in alkaline electrolyte with KNO_3 and CHO, b) the $Ag_4Pd_2(SR)_8$ system in alkaline KNO_3 solution, and c) the Ti_4-^iPrOH system in alkaline KNO_2 solution, respectively. In situ ATR-FTIR spectra obtained from d) electrochemical synthesis of CHOX on the Ag_4Pd_2-S-Ti_4 catalyst in the alkaline electrolyte with KNO_3 and CHO, e) electrochemical NO_3^- reduction on the $Ag_4Pd_2(SR)_8$ cluster in alkaline KNO_3 solution, and f) electrochemical NO_2^- reduction on the Ti_4-^iPrOH cluster in alkaline KNO_2 solution, respectively.

(Figure 5a), the bands from $*NO_2^-$ species shifted to 1273 and 1446 cm^{-1}, and the band from $*NH_2OH$ species shifted to 922 cm^{-1}, yet the $*HNH$ was not detected. It showed that $*NH_2OH$ was desorbed from the catalyst surface and then captured by CHO to produce the CHOX, preventing the system from generating NH_3.

As a control, Raman spectra were measured in alkaline KNO_3 solution without/with CHO using $Ag_4Pd_2(SR)_8$ as a reference catalyst. The band from adsorbed $*NO_3^-$ species shifted to 1010 cm^{-1} and the bands from the $*NO_2^-$ species were located at 1272 and 1444 cm^{-1} (Figure 5b). Combination with the vibrational signals of Figure S24b, it showed that the addition of CHO did not affect the NO_3^- reduction to NO_2^- on the $Ag_4Pd_2(SR)_8$. For the Raman spectra of Ti_4-^iPrOH in alkaline KNO_2 electrolyte (Figure 5c), besides the characteristic signals of Ti_4-^iPrOH catalyst, three weak bands at 922, 1390, and 1439 cm^{-1} assigned to $*NH_2OH$, $*HNH$, and $*NO_2^-$ species,[49] respectively, were observed. In particular, the faint signals of the by-product $*NH_3$ were detected at 1147 cm^{-1}.[12] Combined with the above analysis, we further discovered that the metal cluster unit of the Ag_4Pd_2-S-Ti_4 catalyst could catalyze the NO_3^- reduction to NO_2^-, while the other polyoxotitanium unit without ^iPrO catalyzed the successive reduction of NO_2^- to NH_2OH, which was consistent with the FTACV results. In addition, we also monitored the Raman spectra of the mechanical mixture of

$Ag_4Pd_2(SR)_8$ and Ti_4-^iPrOH (Figure S24c), where NH_2OH signal was not observed and an out-of-plane bending vibration of NH_3 at 1123 cm^{-1} was detected,[12] which accounted for quite a low efficiency for CHOX synthesis on the mixture.

The potential-dependent intermediate species were further monitored using in situ attenuated total reflection Fourier transform infrared spectroscopy (ATR-FTIR). From the Ag_4Pd_2-S-Ti_4 catalyst system (Figure 5d), the band at 1647 cm^{-1} was assigned to be the δ_{HOH} of water.[5,51] The inverted band at 1440 cm^{-1} was due to the consumption of $*NO_3^-$ source.[51] The bands at 1339 and 1191 cm^{-1} were attributed to the $*NO_2^-$ species, and the band at 1175 cm^{-1} was assigned to generated $*NH_2OH$.[5,51–55] The $*NH_2$ bending vibration was detected at 1540 cm^{-1}.[54] Since no signal associated with CHOX was observed, it again showed that the nucleophilic addition of NH_2OH to CHO occurred in the solution rather than on the catalyst surface. Moreover, the IR spectra of both the NO_3^- reduction on the $Ag_4Pd_2(SR)_8$ cluster and the NO_2^- reduction on the Ti_4-^iPrOH cluster were carried out to validate our proposed catalysis mechanism. As shown in Figure 5e, a negative band at ~1438 cm^{-1} ($*NO_3^-$) and the bands at 1333 and 1199 cm^{-1} ($*NO_2^-$) were observed on the $Ag_4Pd_2(SR)_8$ case, indicating that $Ag_4Pd_2(SR)_8$ could reduce NO_3^- to NO_2^-. For Ti_4-^iPrOH system (Figure 5f), the band intensities of 1199 and 1320 cm^{-1} ($*NO_2^-$) were very weak,[4] while the band at 1175 cm^{-1} from $*NH_2OH$ and the band at 1118 cm^{-1} from $*NH_3$ were observed,[54] indicating that Ti_4-^iPrOH can reduce NO_2^- to NH_2OH and NH_3. Overall, two functional units of the Ag_4Pd_2-S-Ti_4 catalyst originated from the $Ag_4Pd_2(SR)_8$ and Ti_4-^iPrOH could be capable to discriminating between NO_3^- and NO_2^-, leading the former-assisted NO_3^- deoxygenation and the latter-relayed NO_2^- hydrogenation.

Density functional theory (DFT) calculations were performed to provide further insights into the reduction pathways of NO_3^- over the above three catalysts. To simplify the computational models, the ligands of $Ag_4Pd_2(SR)_8$ cluster were replaced with $-SCH_3$, while the tert-butyl groups of Ti_4-^iPrOH were substituted by $-CH_3$ group and the isopropoxy groups were simultaneously removed (Figure S25). In the meantime, $Ag_4Pd_2(SR)_8$, which had one ligand discarded, was coupled with the Ti_4-^iPrOH cluster without the ^iPrO groups to construct the Ag_4Pd_2-S-Ti_4 catalyst, and the optimized configurations were shown in Figure S26. As displayed from the plot of electron density difference (Figure S27) and Bader charge analysis (Table S3), there was a manifest charge transfer at the cluster–cluster interface. This provided an important indicator for taking the interfacial sites of the coupled Ag_4Pd_2-S-Ti_4 catalyst as active centers for further DFT calculations and mechanism exploration.

The free energy evolution based on the Gibbs free-energy change (ΔG) in the NO_3^- reduction to NH_2OH and the corresponding adsorption configurations were presented in Figure 6. The whole reaction process involved the stepwise deoxygenation to $*NO$ and subsequent hydrogenation steps to produce $*NH_2OH$. Regarding to the $Ag_4Pd_2(SR)_8$ cluster, two metal sites (i.e., Pd and Ag) needed to be considered. As shown in Figure 6a, the rate-determining step (RDS) was
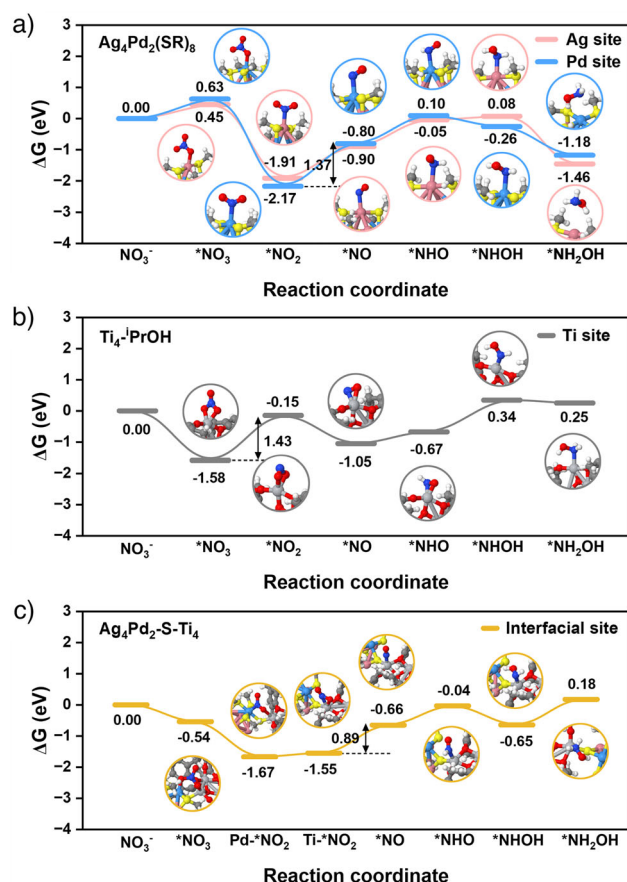
Figure 6. The reduction pathways of NO_3^- to NH_2OH over the three catalysts. Gibbs free energy diagrams of the NO_3^- conversion to NH_2OH over a) the $Ag_4Pd_2(SR)_8$ cluster, b) the Ti_4-^iPrOH cluster, and c) the Ag_4Pd_2-S-Ti_4 catalyst, respectively. Insets showed the optimized configurations of each reaction intermediates in the reaction process. The balls in blue, pink, yellow, red, gray, white, dark blue, and dark gray represented palladium, silver, sulfur, oxygen, titanium, hydrogen, nitrogen and, carbon atoms, respectively.

the reduction of $*NO_2$ to $*NO$ for both two metal sites, with the Pd site exhibiting a higher energy barrier than the Ag site in the reduction of $*NO_2$ to $*NO$. In comparison, the Ti site possessed greater advantage in the adsorption of $*NO_3$ ($\Delta G = -1.58$ eV) (Figure 6b), where two oxygen atoms of NO_3^- were bridged to one Ti site. Nevertheless, the conversion from $*NO_3$ to $*NO_2$ on the Ti_4-^iPrOH cluster was identified as the RDS, with a huge ΔG uphill of 1.43 eV. Considering more stability of NO_2^- species on the Pd site than that on the Ag site, the ΔG of the NO_3^- reduction process on the Ag_4Pd_2-S-Ti_4 catalyst was calculated in terms of the interfacial sites containing the Ti—S—Pd domain. As shown in Figure 6c, one O atom in $*NO_3$ was adsorbed to the Pd site and the other O atom was adsorbed to the Ti site. Since $*NO_3$ was deoxygenated, the N atom of $*NO_2$ was attached to the Pd site, and subsequently the N atom was desorbed from the Pd site and $*NO_2$ was transferred to the Ti site. The deoxygenation and hydrogenation of $*NO_2$ occurred on the Ti site and $*NO$ species stood on the Ti site, which was completely different from the adsorption patterns on isolated $Ag_4Pd_2(SR)_8$ and Ti_4-^iPrOH cases. As a result, the entire

reaction pathway of the NO_3^- reduction to NH_2OH in the Ag_4Pd_2-S-Ti_4 system was much smoother than that on either $Ag_4Pd_2(SR)_8$ or Ti_4-^iPrOH, and the corresponding RDS was $*NO_2$ to $*NO$ with a much lower ΔG value of 0.89 eV. The calculation studies further elucidated the distinctive roles of the interfacial Ti—S—metal sites interconnected with the two functional units in the synthesis of crucial NH_2OH species, in which each unit could endeavor to perform its respective contribution to the reduction processes of NO_3^- source.

Conclusion

In summary, we have pioneered the design strategy for constructing the unique proximity of the two active sites severally from metal cluster and polyoxotitanium cluster, thereby combining the functions of two monomers into one catalyst to achieve highly catalytic activity and high selectivity of the target product. The heterodimeric Ag_4Pd_2-S-Ti_4 catalyst exhibited a remarkably synergistic performance for CHOX synthesis, outperforming the two monomers. The Ti—S—metal interface within the Ag_4Pd_2-S-Ti_4 catalyst was demonstrated to be crucially catalytic sites, where the NO_3^- reduction to NO_2^- performed on the metal sites and the NO_2^- species then flipped to the Ti site to continue the reduction to produce hydroxylamine, and the CHOX synthesis was finally accomplished via the coupling of the hydroxylamine and cyclohexanone in the solution. This work would open up enormous possibilities for the access to currently elusive metal-support interactions of heterogeneous catalysts, helping to realize functional modules of the heterodimeric catalysts to execute their own tasks in chemical bond constructions.

Conflict of Interests

The authors declare no conflict of interest.

Data Availability Statement

The data that support the findings of this study are available in the Supporting Information of this article.

[1] R. Mokaya, M. Poliakoff, *Nature* **2005**, *437*, 1243–1244.

[2] B. Zong, B. Sun, S. Cheng, X. Mu, K. Yang, J. Zhao, X. Zhang, W. Wu, *Engineering* **2017**, *3*, 379–384.

[3] J. Sharp, A. Ciotti, H. Andrews, S. R. Udayasurian, M. García-Melchor, T. Li, *ACS Catal.* **2024**, *14*, 3287–3297.

[4] R. Zhao, Y. Wang, J. Fu, F. Zhang, L. Wen, Y. Zhao, B. Guan, B. Han, Z. Liu, *J. Am. Chem. Soc.* **2024**, *146*, 27956–27963.

[5] Y. Wu, J. Zhao, C. Wang, T. Li, B. H. Zhao, Z. Song, C. Liu, B. Zhang, *Nat. Commun.* **2023**, *14*, 3057.

[6] L. Luo, L. Li, L. Xu, Y. Yan, S. Zhang, H. Zhou, Z. Li, M. Shao, X. Duan, *CCS Chem.* **2025**, *7*, 266–278.

[7] S. Han, H. Li, T. Li, F. Chen, R. Yang, Y. Yu, B. Zhang, *Nat. Catal.* **2023**, *6*, 402–414.

[8] X. Zhang, C. Wang, Y. Guo, B. Zhang, Y. Wang, Y. Yu, *J. Mater. Chem. A* **2022**, *10*, 6448–6453.

[9] J. Shao, Y. F. Zhang, S. Z. Xue, Z. Y. Li, X. Li, B. Liang, T. Z. Li, H. Dong, Y. W. Zhang, *Inorg. Chem. Front.* **2024**, *11*, 5286–5298.

[10] X. Lan, C. Cheng, C. Guo, M. Guo, T. Li, Y. Wu, Y. Yu, B. Zhang, *Sci. China Chem.* **2023**, *66*, 1758–1762.

[11] L. Liu, S. J. Zheng, H. Chen, J. Cai, S. Q. Zang, *Angew. Chem. Int. Ed.* **2024**, *63*, e202316910.

[12] W. Gao, K. Xie, J. Xie, X. Wang, H. Zhang, S. Chen, H. Wang, Z. Li, C. Li, *Adv. Mater.* **2023**, *35*, 2202952.

[13] J. Zhou, S. Han, R. Yang, T. Li, W. Li, Y. Wang, Y. Yu, B. Zhang, *Angew. Chem. Int. Ed.* **2023**, *62*, e202305184.

[14] X. Cai, H. Wang, Y. Tian, W. Ding, Y. Zhu, *ACS Catal.* **2024**, *14*, 11918–11930.

[15] R. Jin, G. Li, S. Sharma, Y. Li, X. Du, *Chem. Rev.* **2021**, *121*, 567–648.

[16] N. Li, J. J. Liu, J. W. Sun, B. X. Dong, L. Z. Dong, S. J. Yao, Z. Xin, S. L. Li, Y. Q. Lan, *Green Chem.* **2020**, *22*, 5325–5332.

[17] N. Li, J. M. Lin, R. H. Li, J. W. Shi, L. Z. Dong, J. Liu, J. He, Y. Q. Lan, *J. Am. Chem. Soc.* **2023**, *145*, 16098–16108.

[18] Y. Q. Tian, W. L. Mu, L. L. Wu, X. Y. Yi, J. Yan, C. Liu, *Chem. Sci.* **2023**, *14*, 10212–10218.

[19] M. Zhou, C. Zeng, Y. Chen, S. Zhao, M. Y. Sfeir, M. Zhu, R. Jin, *Nat. Commun.* **2016**, *7*, 13240.

[20] J. Zhang, Z. Li, J. Huang, C. Liu, F. Hong, K. Zheng, G. Li, *Nanoscale.* **2017**, *9*, 16879–16886.

[21] G. Li, X. Sui, X. Cai, W. Hu, X. Liu, M. Chen, Y. Zhu, *Angew. Chem. Int. Ed.* **2021**, *60*, 10573–10576.

[22] T. Song, B. Ge, C. Juan, S. Huang, D. Li, Q. Zhai, X. Cai, X. Liu, W. Ding, Y. Zhu, *CCS Chem.* **2025**, *7*, 731–739.

[23] Q. Li, Y. Tan, B. Huang, S. Yang, J. Chai, X. Wang, Y. Pei, M. Zhu, *J. Am. Chem. Soc.* **2023**, *145*, 15859–15868.

[24] G. Hu, Z. Wu, D. e. Jiang, *J. Mater. Chem. A* **2018**, *6*, 7532–7537.

[25] W. Zhao, Y. Li, W. Shen, *Chem. Commun.* **2021**, *57*, 6838–6850.

[26] S. Zhu, S. Ma, D. Song, Y. Wang, J. Lu, T. Ai, H. Lu, S. He, Y. Luo, *Chem. Eng. J.* **2024**, *489*, 151289.

[27] W. Zhang, L. Cai, S. Cao, L. Qiao, Y. Zeng, Z. Zhu, Z. Lv, H. Xia, L. Zhong, H. Zhang, X. Ge, J. Wei, S. Xi, Y. Du, S. Li, X. Chen, *Adv. Mater.* **2019**, *31*, 1906156.

[28] X. Liu, J. Yuan, J. Chen, J. Yang, Z. Wu, *Part. Part. Syst. Charact.* **2019**, *36*, 1900003.

[29] Y. Q. Tian, Y. S. Cui, J. H. Zhu, C. Q. Xu, X. Y. Yi, J. Li, C. Liu, *Chem. Commun.* **2022**, *58*, 9034–9037.

[30] Y. Q. Tian, L. F. Dai, W. L. Mu, W. D. Yu, J. Yan, C. Liu, *Chem. Sci.* **2023**, *14*, 14280–14289.

[31] Y. Pu, H. Xie, X. He, J. Lv, Z. Zhu, J. Hong, K. Zeng, J. Hu, G. Yang, *Polymer.* **2022**, *252*, 124948.

[32] X. Wang, Y. Yu, Z. Wang, J. Zheng, Y. Bi, Z. Zheng, *Inorg. Chem.* **2020**, *59*, 7150–7157.

[33] X. Xu, S. Li, D. Wu, R. Gu, *ACTA Chim. Sinica.* **2007**, *65*, 1095–1100.

[34] C. K. A. Nyamekye, S. C. Weibel, E. A. Smith, *J. Raman Spectrosc.* **2021**, *52*, 1246–1255.

[35] A. L. Let, D. E. Mainwaring, C. Rix, P. Murugaraj, *J. Non-Cryst. Solids.* **2008**, *354*, 1801–1807.

[36] M. A. Sriram, P. N. Kumta, *J. Mater. Chem.* **1998**, *8*, 2441–2451.

[37] Z. Gao, Y. Jian, S. Yang, Q. Xie, C. J. Ross Mcfadzean, B. Wei, J. Tang, J. Yuan, C. Pan, G. Yu, *Angew. Chem. Int. Ed.* **2023**, *62*, e202304173.

[38] X. Liu, J. Feng, X. Cheng, J. Zhang, J. Huo, D. Chen, A. Marcomini, Y. Li, Q. Xu, J. Lu, *Adv. Funct. Mater.* **2024**, *34*, 2400892.

[39] Y. Wang, H. Li, W. Zhou, X. Zhang, B. Zhang, Y. Yu, *Angew. Chem. Int. Ed.* **2022**, *61*, e202202604.

[40] L. Ma, Y. Miao, J. Yang, Y. Fu, Y. Yan, Z. Zhang, Z. Li, M. Shao, *Adv. Energy Mater.* **2024**, *14*, 2401061.

[41] Y. Liu, Z. Yang, Y. Zou, S. Wang, J. He, *Energy Environ. Mater.* **2024**, *7*, e12576.

[42] P. Zhou, X. Lv, S. Tao, J. Wu, H. Wang, X. Wei, T. Wang, B. Zhou, Y. Lu, T. Frauenheim, X. Fu, S. Wang, Y. Zou, *Adv. Mater.* **2022**, *34*, 2204089.

[43] R. Z. Snitkoff-Sol, A. M. Bond, L. Elbaz, *ACS Catal.* **2024**, *14*, 7576–7588.

[44] Y. Zhang, A. N. Simonov, J. Zhang, A. M. Bond, *Curr. Opin. Electrochem.* **2018**, *10*, 72–81.

[45] S. Wang, W. Huo, F. Fang, Z. Xie, J. K. Shang, J. Jiang, *Chem. Eng. J.* **2022**, *429*, 132410.

[46] S. Wang, B. Xu, W. Huo, H. Feng, X. Zhou, F. Fang, Z. Xie, J. K. Shang, J. Jiang, *Appl. Catal. B.* **2022**, *313*, 121472.

[47] X. Zhang, X. Sun, S. X. Guo, A. M. Bond, J. Zhang, *Energy Environ. Sci.* **2019**, *12*, 1334–1340.

[48] D. M. L. Goodgame, M. A. Hitchman, *Inorg. Chem.* **1965**, *4*, 721–725.

[49] J. Y. Fang, Q. Z. Zheng, Y. Y. Lou, K. M. Zhao, S. N. Hu, G. Li, O. Akdim, X. Y. Huang, S. G. Sun, *Nat. Commun.* **2022**, *13*, 7899.

[50] D. P. Butcher, A. A. Gewirth, *Nano Energy.* **2016**, *29*, 457–465.

[51] S. Jia, L. Wu, X. Tan, J. Feng, X. Ma, L. Zhang, X. Song, L. Xu, Q. Zhu, X. Kang, X. Sun, B. Han, *J. Am. Chem. Soc.* **2024**, *146*, 10934–10942.

[52] S. Jia, X. Tan, L. Wu, X. Ma, L. Zhang, J. Feng, L. Xu, X. Song, Q. Zhu, X. Kang, X. Sun, B. Han, *Chem. Sci.* **2023**, *14*, 13198–13204.

[53] Y. Tang, Z. Jiang, Z. Yuan, L. Xu, C. Jin, B. Chen, Z. Lin, J. Zao, J. Du, X. Zhang, X. Gao, Y. Liang, *Nat. Commun.* **2024**, *15*, 9800.

[54] R. Zhang, C. Li, H. Cui, Y. Wang, S. Zhang, P. Li, Y. Hou, Y. Guo, G. Liang, Z. Huang, C. Peng, C. Zhi, *Nat. Commun.* **2023**, *14*, 8036.

[55] Y. Cheng, S. Liu, J. Jiao, M. Zhou, Y. Wang, X. Xing, Z. Chen, X. Sun, Q. Zhu, Q. Qian, C. Wang, H. Liu, Z. Liu, X. Kang, B. Han, *J. Am. Chem. Soc.* **2024**, *146*, 10084–10092.

Research Article

Cyclohexanone Oxime Electrosynthesis

T. Song, C. Shen, Y. Tian, Q. Zhai, S. Tang,
Y. Zhu* —————————— e202507569

A Heterodimeric Cluster-Based Pair
Catalyst for Electrochemical Synthesis of
Cyclohexanone Oxime

We report a design strategy for
constructing the unique proximity of
the two active sites severally from metal
cluster and polyoxotitanium cluster,
thereby combining the functions of two
cluster monomers into one catalyst to
achieve highly catalytic activity while
simultaneously increasing the target
product selectivity.